Chapter 4

Block copolymer melts confined under moving parallel walls

4.1 Introduction

For many decades, the microphase separation of block copolymer (BCP) melts [126–130] has been a subject of significant interest in research fields [95,131–134]. A BCP chain (A_nB_m) is a long chain molecule composed of two segments, one with n A-type monomers and the other with m B-type monomers, which are covalently bonded to one another. After quenching the temperature below the critical point, a homogeneous mixture of BCP melt enters a thermodynamically unstable regime. Consequently, the system undergoes phase separation, forming distinct A-rich and B-rich domains [1,6,135]. The bond constraint between two incompatible blocks dictates the spatial extent of the domains, resulting in the formation of microscopic regions that are either A-rich or B-rich. During coarse-graining, the BCP melt can develop various morphologies, such as gyroids, cylinders, spheres, and lamellae, depending on the ratio of the lengths of its subchains ($n : m$ [126–129].

The morphologies developed during the self-assembly of BCP melts have become a topic of significant interest due to their rapidly expanding essential applications in various fields such as advanced materials [136], lithography [136–138], drug delivery [136,139,140], and porous materials [136,141]. The more recent applications of BCPs come from their self-assembly at the nanoscale; these properties rely on the long-range order of BCP melts [142]. The morphology change significantly impacts the final properties of multiphase materials, with domain coarsening having a substantial influence on material properties.

One can generate new and advanced materials with significant industrial applications by tuning the morphology at the molecular scale. Recent studies have developed various methods to accelerate the phase separation kinetics of BCP melt systems. These methods include the application of shear [143], electric fields [144], chemically patterned substrate [145], etc. Among these, the use of either steady or oscillatory shear is the most straightforward approach [146]. The application of shear plays a dominant role in controlling the resulting morphologies. Various interesting structures, such as spherical, cylindrical, and lamellar morphologies, have been achieved using these methods [147–152]. In some recent works, using the thin films, the degree of alignment of the cylindrical [153] and spherical evolution [154] has been improved using shear. It is believed that on the application of shear, the microphases try to minimize the effect of shear within the system, so they try to reorient themselves concerning symmetry-breaking shear flow [146]. Most of these studies have primarily focused on $2d$ surfaces [143,146], such as thin films/substrates [153,154], or the steady-state properties [155,156] of small BCP melt systems [147–152]. Consequently, a detailed DPD simulation study of the phase separation kinetics of $3d$ BCP melts under shear is still lacking. Additionally, understanding the competition between domain coarsening and applied shear, as well as the impact of physical boundaries, is crucial for comprehending the resulting morphology and related properties [146].

Thus, studying the effect of different shear rates on the phase segregation kinetics of BCP melts is of paramount importance in confined systems. We have considered a BCP melt system confined from the top and bottom by two solid walls with an amorphous arrangement. A symmetric BCP melt system with equal chain lengths of the two incompatible blocks is used. Shear is introduced by moving the walls in a particular direction. As both walls have similar interactions with each subchain, the amount of shear experienced by both phases is equal. Hence, it is reasonable to investigate the influence of shear on the kinetics of microphase separation in BCP melts. We are examining the impact of shear on the segregation process in the bulk system, specifically whether shear stimulates or delays this process. Additionally, we are analyzing how microscale morphologies differ at low and high shear rates. Lastly, we aim to understand the potential effects on scaling functions and growth laws.

In this chapter, shear is generated in various scenarios depending on the direction of wall motion: (i) Both walls are kept stationary, (ii) only the top wall moves while the bottom wall remains fixed, (iii) both walls move in positive x-direction, and (iv) both walls move in opposite directions. The DPD simulation technique is used to analyze the effect of applied shear. However, replicating these scenarios experimentally can be challenging. The experimental study of case (ii) may be feasible using various methods, including fabricating polymer membrane casting [157], flat-sheet membranes [153,154], nano-structuring in gelled emulsions [158,159], flow-induced crystallization [160], and bulk BCP melts [161]. To the best of our knowledge, there is no experimental evidence related to case (iii). Nonetheless, this simulation study can offer valuable insights into phenomena that may be difficult to investigate theoretically or experimentally. By considering the limitations and feasibility of experimental methods, simulation studies of complex systems can help bridge the gap between theory and experiments. Furthermore, future research will prioritize the development of innovative experimental methods to replicate these challenging scenarios and substantiate simulation findings accurately.

4.2 System details

In this research, we explore the impact of shear on the phase separation dynamics of a BCP melt system. A cubic simulation box is utilized with dimensions (dimensionless units): $L_x \times L_y \times L_z = 64 \times 64 \times 64$. The number density of the system is taken as $\rho = 3$. Consequently, the total number of DPD beads taken in the system is $N = \rho \times L^3 = 7,86,432$. We have taken a symmetric BCP melt A_nB_m with an equal number of beads in each subchain as $n : m = 1 : 1$. The chain length of each BCP molecule is taken as $l_p = 32$ (degree of polymerization). Total number of A- and B-type beads is $N_A = N_B = 3,80,928$ ($\phi_A = \phi_B = 4.843 \times 10^{-1}$), resulting the densities of A and B beads, $\rho_A = \rho_B = 1.453$. This implies the total number of BCP chains is $N_{BCP} = 23,808$. The system is confined from the top and bottom with solid walls, whereas the periodic boundary conditions are applied only along x- and y-directions. The height of each wall is taken as $h = 1.0$. We can calculate the number of wall beads and their volume fraction as: $N_w = 24,576$, and $\phi_w = 3.125 \times 10^{-2}$

When both walls are stationary, the velocity components of the walls v_{wx}, v_{wy}, and v_{wz} are zero (case 1). To apply shear, the walls are given a constant velocity along the x-direction, $\vec{v}_w = (v_{wx}, v_{wy} = 0, v_{wz} = 0)$. To study the effect of shear, three scenarios are considered based on the direction of the wall's motion: (i) the top wall moves in the positive x-direction (case 2) with $v_{wx} = 0.1$, 0.5, and 1.0, while the bottom wall remains fixed. (ii) Both the top and bottom walls move in the same direction (case 3) with the same velocities as in case 2. (iii) Both walls move in opposite directions (the top wall is allowed to move in the positive x-direction whereas the bottom wall in the negative x-direction); this is defined as case 4. A bounce-back boundary condition is applied at the wall-BCP interfaces to prevent the BCP beads from penetrating the solid walls [162]. Consequently, we have applied no-slip boundary conditions with minimal interfacial density oscillation [163,164]. For different wall velocities, $v_{wx} = 0.1$, 0.5, and 1.0, the corresponding shear rates are $\dot{\gamma} = 1.56 \times 10^{-3}$, 7.80×10^{-3}, and 1.56×10^{-2}, respectively. Thus, the applied shear rate ranges from $\dot{\gamma} = 1.8 \times 10^{5}/s$ to $1.8 \times 10^{6}/s$. This range of applied shear is consistent with the high shear rates used in microfluidic device experiments [165,166].

In our simulation modeling, we started with a symmetric BCP melt $(A_nB_n; n = 16)$ confined between two rigid walls at the top and bottom of the simulation box, oriented along the transverse z-direction. Initially, we equilibrated the system at a high temperature ($T = 5$) for $t = 2 \times 10^{5}$ simulation time steps to achieve a homogeneously mixed state, with zero external shear applied during this period. After resetting the time step to zero, we quenched the system to a lower temperature ($T = 1$). During the subsequent coarsening phase, we allowed the walls to move in specific directions with various shear rates depending on the scenario. To ensure accurate averaging, we conducted five independent simulation runs for scaling and growth laws and ten for velocity profile and viscosity calculations. We monitored the evolution, characterization functions, growth laws, anisotropy development, viscosity, velocity profile, and other relevant parameters across different shear rates in all cases.

4.3 Calculaion of velocity profile and shear-viscosity

First, we calculate the average velocity profile of the system for different scenarios of applied shear. Since an additional velocity is given to the wall particles along the x-direction, the x-component of velocity is crucial in the average velocity profile. As the walls move along the x-direction with a constant velocity v_{wx}, a shear rate $\dot{\gamma}$ is applied to the system. The effect of moving walls at different shear rates is clearly visible along the vertical direction. Therefore, we calculate the velocity profile along the z-direction. To do this, we divide the system into thin slabs of unit thickness ($\Delta z = 1.0$) along the vertical direction. Then, we compute the average velocity components $\langle v_x \rangle$, $\langle v_y \rangle$, and $\langle v_z \rangle$ of all particles within each slab [167,168]. Since no additional velocity is along the y and z directions, we obtain $\langle v_y \rangle = \langle v_z \rangle = 0$ for all cases. Therefore, we focus on calculating the x component of velocity and plot the graph of $\langle v_x \rangle$ vs. z to visualize the velocity profile for different scenarios of applied shear.

We calculate the viscosity using the reverse non-equilibrium molecular dynamics (RNEMD) technique to demonstrate the effect of shear. This method was developed by Müller-Plathe [64,167,168] and is further discussed in various studies. In this technique, a momentum flux is imposed on the system along the z-direction (specifically in our case) by exchanging momentum between particles. A real momentum flux is generated in the opposite direction in response to this imposed unphysical momentum flux. Consequently, a velocity profile develops in the vertical direction. We can calculate the velocity profile as discussed earlier. The viscosity can then be determined using the following equation:

$$j_z(p_x) = -\eta \left(\partial v_x / \partial z \right). \tag{4.1}$$

Here, η is the viscosity, $j_z(p_x)$ is the momentum flux and $\partial v_x / \partial z$ is the velocity profile along z-direction.

4.4 Anisotropy parameter

Further, the anisotropy parameter $D_{xy}(t)$ is calculated using the following relation to evaluate the anisotropic degree of evolved morphology [169,170].

$$D_{xy}(t) = \frac{\sum (k_x^2 - k_y^2)/k^2) S(k_x, k_y, k_z)}{\sum S(k_x, k_y, k_z)}. \tag{4.2}$$

Here, k_x and k_y are the components of wave vector $\vec{k}$ in the xy-plane for a fixed k_z where $k^2 = k_x^2 + k_y^2 + k_z^2$, and $S(k_x, k_y, k_z)$ denotes the structure factor at a point (k_x, k_y, k_z) in Fourier space. $D_{yz}(t)$, and $D_{xz}(t)$ are also calculated in the yz and xz planes, respectively in the same faison. From the recent studies, the anisotropy parameters should have value $D_{ij} \simeq 0$ for a perfect isotropic system and $D_{ij} \to 1$ for a fully anisotropic system.

4.5 Effect of external shear on viscosity and velocity profile

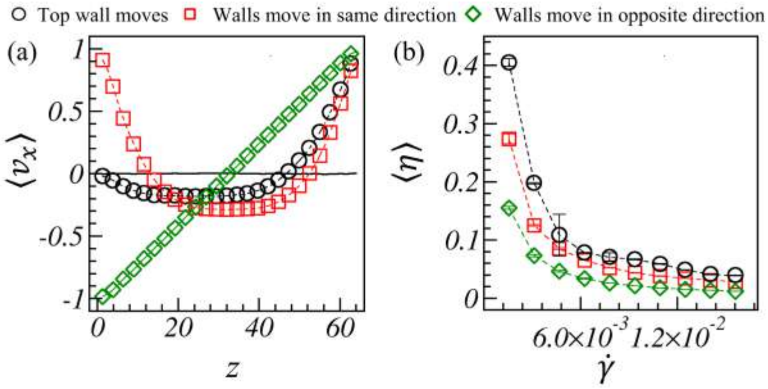

Fig. 4.1: (a) Plots of the average velocity profile, $\langle v_x \rangle$ vs. z, at a high shear rate ($\dot{\gamma} = 1.56 \times 10^{-2}$), with different symbols representing the various scenarios. (b) Plots of shear viscosity, $\langle \eta \rangle$, vs. $\dot{\gamma}$ at the late time step ($t = 5 \times 10^3$) for all three scenarios, each indicated by distinct symbols.

To start, we plot the average velocity profile across the vertical direction for different scenarios. In Fig. 4.1(a), $\langle v_x \rangle$ vs z is shown for all cases at the late time ($t = 5 \times 10^3$). The solid black line represents the velocity profile for case 1. With $\dot{\gamma} = 0.0$, we see that $\langle v_x \rangle = 0.0$, indicating the conservation of linear momentum. The curve with black symbols represents case 2, where only the top wall moves at $\dot{\gamma} = 1.56 \times 10^{-2}$. Here, the velocity profile is maximum near the top wall, decreases to a negative value with distance, and gradually approaches zero near the bottom wall. In case 3 (red curve), the velocity profile decreases smoothly with increasing distance from both walls, which move in the positive x-direction and reach a negative minimum at the center of the box. In case 4 (green curve), the top wall is allowed to move in the positive x-direction, whereas the bottom wall moves in the negative x-direction. Consequently, the velocity profile increases linearly with z from 1 to L, crossing zero at $L/2$.

In Fig. 4.1(b), we plot the average shear viscosity $\langle \eta \rangle$ against $\dot{\gamma}$ at a late evolution time of $t = 5 \times 10^3$. Different symbols represent the various scenarios studied. The averages over ten ensembles are denoted by $\langle \cdots \rangle$. In each plot, we observe a decrease in viscosity with increasing shear rates, indicative of shear thinning behavior, which further saturates at high $\dot{\gamma}$ values. Consequently, the average domain size $R(t)$ decreases at high shear rates for cases 2-4. The viscosity is lowest in case 4 compared to cases 2 and 3, highlighting the more pronounced effect of shear in this scenario.

4.5.1 Velocity profile depends on different parameters

First, we examine the reason for obtaining negative values in the central region of the velocity profile. Thus, we plot the velocity profile in Fig. 4.2 by varying different parameters for cases 2 and 3. It is notable that the moving walls generate a flow field in the adjacent layers of separating polymers. As the distance from the sheared walls increases, the effect decreases. These flow fields eventually decay to zero at a certain distance from the wall, such as ($z \approx 48$ for case 2 in Fig. 4.2(a), and $z \approx 12$ and 52 for case 3 in Fig. 4.2(d)). Note that the system adheres to the incompressible Newtonian flow field condition, inducing a momentum flow in the opposite direction in response to the non-equilibrium situation to maintain momentum conservation throughout the system [167,168,171].

Without external shear, linear momentum conservation occurs automatically in DPD simulations. However, when shear is applied to the top walls, the shear stress causes

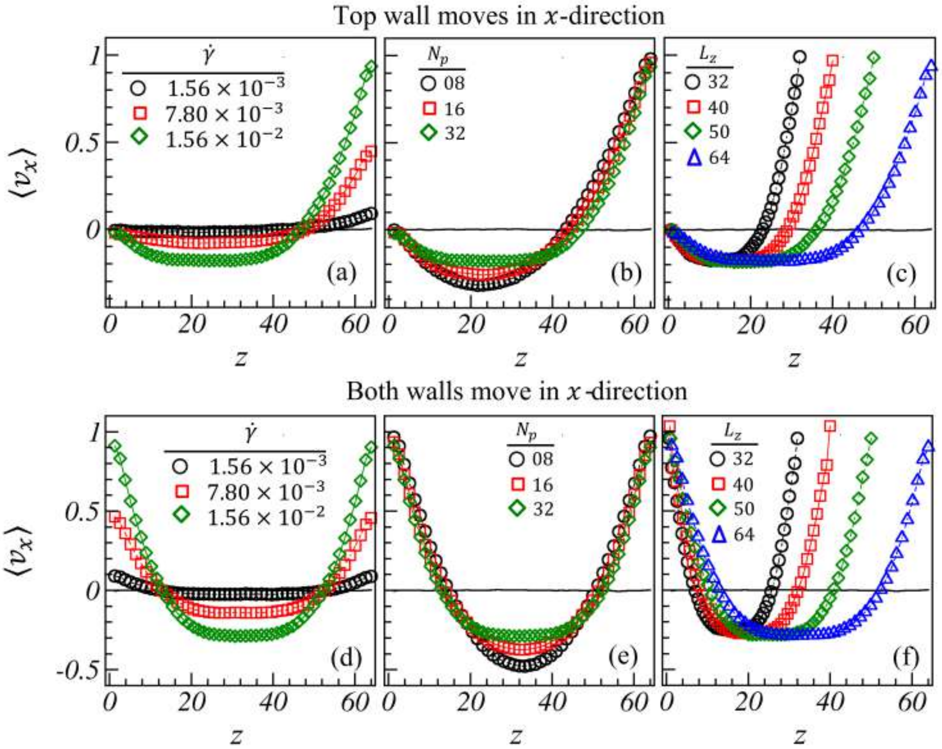

Fig. 4.2: (a-c) Plots for the velocity profile, $\langle v_x \rangle$ along z-direction. (a) $\langle v_x \rangle$ vs. z at different shear rates mentioned in the legend at a fixed chain length, $N_p = 32$. (b) Effect of BCP chain length on $\langle v_x \rangle$ vs. z at a fixed shear rate, $\dot{\gamma} = 1.56 \times 10^{-2}$. The three black, red, and green curves represent the data for chain length $N_p = 8$, 16, and 32, respectively. In (a) and (b), The height of the box is fixed at $L = 64$ in a cubic simulation box. We vary the height of the box in (c) and compare the velocity profile by keeping the box length ($L = 64$) fixed in x- and y-directions at $\dot{\gamma} = 1.56 \times 10^{-2}$ and $N_p = 32$. In (d-f), the velocity profiles are plotted for case 3 with the variation of the same set of parameters as discussed in (a-c).

the layers of the BCP melt system to slide over each other. This generates a flow field and forms different layers parallel to the top wall. The layer closest to the moving walls experiences the maximum shear effect, while the layer near the fixed bottom wall experiences the minimum effect. To preserve the Newtonian flow field condition, the net flow in the system must be zero [43,63,67]. Therefore, in case 2, the faster flow in the upper part must be compensated by a slower flow near the bottom wall. Consequently, a negative velocity profile is generated in the central box area, with particle velocities less than the average velocity of the BCP melt. This is due to the shear-induced alignment of the BCP melt system in response to the external shear, leading to the conservation of linear momentum by generating a velocity gradient along the height of the box. In case three, the velocity is highest near the walls and decreases towards the center. Again, a negative velocity profile is observed at the center of the box to conserve linear momentum. In case four, the walls move in opposite directions with the same velocity. This opposite motion balances the net flow in the system, thus conserving linear momentum. Consequently, the velocity profile increases linearly from bottom to top, crossing zero at $z = L/2$.

As we increase the shear rate, the momentum generated in the opposite direction also rises. Consequently, we observe more pronounced negative values in the velocity profile with increasing shear rates, as illustrated in Figs. 4.2(a) and 4.2(d) [167,168,171]. Next, we vary the chain length of the critical BCP melt with $N_p = 8, 16,$ and 32 while keeping the shear rate constant at $\dot{\gamma} = 1.56 \times 10^{-2}$. In Figs. 4.2(b) and 4.2(e), we plot the velocity profile for the BCP melt with different chain lengths. For higher degrees of polymerization of BCP chains, the diffusive transport is slower since the diffusion coefficient, $D \sim N_p^{-\nu}$, where $\nu = 1/2$ is the size exponent in the melt [23,172,173]. Thus, with an increase in chain length, the magnitude of the opposing momentum decreases. Consequently, the magnitude of the negative velocity profile diminishes for longer chain lengths, as illustrated by the black, red, and green curves for $N_p = 8, 16,$ and 32, respectively. In Figs. 4.2(c) and 4.2(f), we vary the distance between the walls and plot $\langle v_x \rangle$ versus z for a fixed shear rate $\dot{\gamma} = 1.56 \times 10^{-2}$ and chain length $N_p = 32$. We observe that the equilibrium wall distance has an insignificant impact on the magnitude of the negative velocity profile.

In Fig. 4.3, we display the average velocity profile over time for cases 2-4. In Figs. 4.3(a)-4.3(c), we vary the shear rate, indicated by different symbols in the legends, and calculate the velocity profile for a slab of unit thickness near the top wall. As time

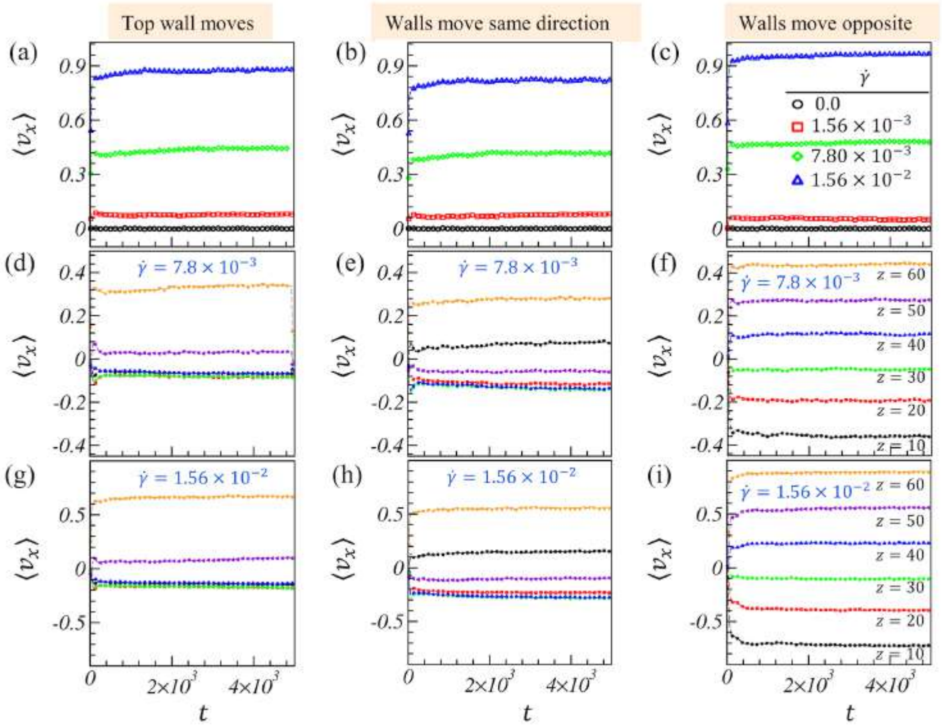

Fig. 4.3: Plots for average velocity profile against time for all three cases of applied shear are mentioned at the top. (a-c) Plots for $\langle v_x \rangle$ vs. t for different shear rates mentioned in the legends. Data is taken at a plane near the top wall. In (d-f) $\langle v_x \rangle$ is plotted at different xy-planes for a moderate shear rate $\dot{\gamma} = 7.8 \times 10^{-3}$. (g-i) plots the same data set as in (d-f), for high shear rate $\dot{\gamma} = 1.56 \times 10^{-2}$.

progresses, the velocity profile rapidly stabilizes to a finite value, with higher shear rates resulting in a greater magnitude of the stabilized velocity profile. Additionally, we compute the velocity profile for different slabs parallel to the walls at shear rates of $\dot{\gamma} = 7.8 \times 10^{-3}$ in Figs. 4.3(d)-4.3(f) and $\dot{\gamma} = 1.56 \times 10^{-2}$ in Figs. 4.3(g)-4.3(i). As we move from top to bottom, the velocity profile exhibits the same behavior discussed in Figs. 4.3(a)-4.3(c); it quickly stabilizes to a finite value over time. The magnitude of the stabilized velocity profile varies depending on the applied shear rates in different scenarios.

4.6 Average bond length and instantaneous temperature

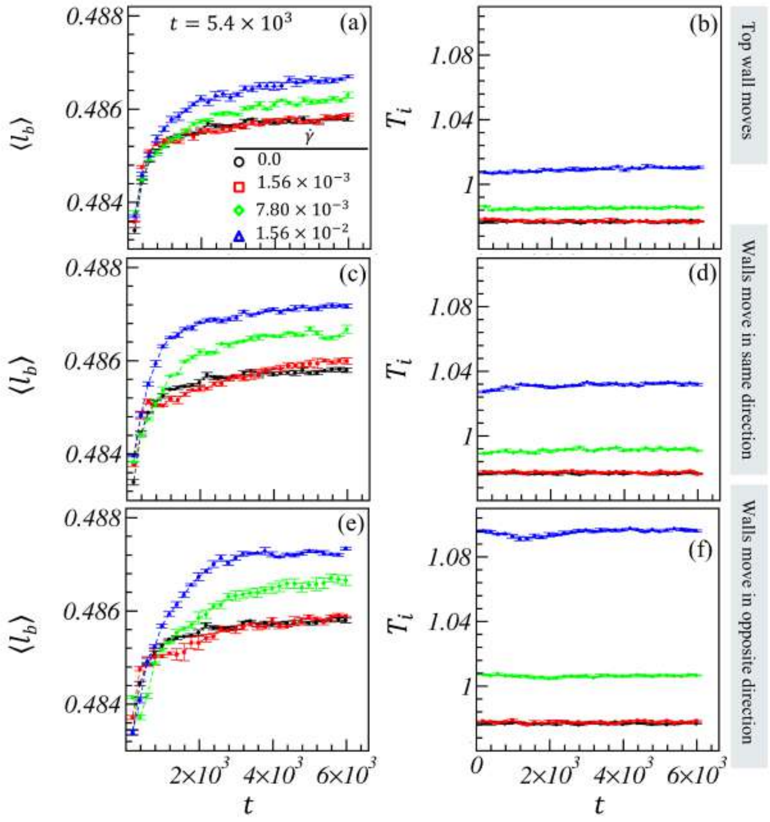

Fig. 4.4: (a), (c), and (e) represent the time-dependent average bond length $\langle l_b \rangle$ for cases 2-4 mentioned at extreme right. Various symbols in the legends represent the different shear rates applied to the system. In the second column (b), (d), and (f), we plotted the instantaneous temperature over time for the same cases as in the first column.

In Figs. 4.4(a), 4.4(c), and 4.4(e), we plot the average bond length over time for cases 2-4, respectively. Different symbol types in the legends represent the shear rates applied to the system. As the shear rate increases, bond stretching also increases, reaching optimum values in case 4 (Fig. 4.4(e)). This bond stretching results from the perturbation of polymer chains under shear, leading to shear thinning in the system. Additionally, we can compute the normalized radius of gyration of BCP chains under different shear rates to further demonstrate the shear thinning behavior caused by the perturbation of polymer chains under shear [174]. The induced momentum flow in opposite directions ensures the conservation of linear momentum within the system. This exchange of momentum also aids in dissipating the excess heat generated by friction [167]. Consequently, only a tiny increase in instantaneous temperature is observed, with T_i ranging from 0.98 to 1.095. Given that the quench temperature is $T_i = 1.0$, it is noteworthy that the variation in instantaneous temperature remains within the statistical error for all cases, as shown in Figs. 4.4(b), 4.4(d), and 4.4(f).

4.7 Case 1: Both walls fixed

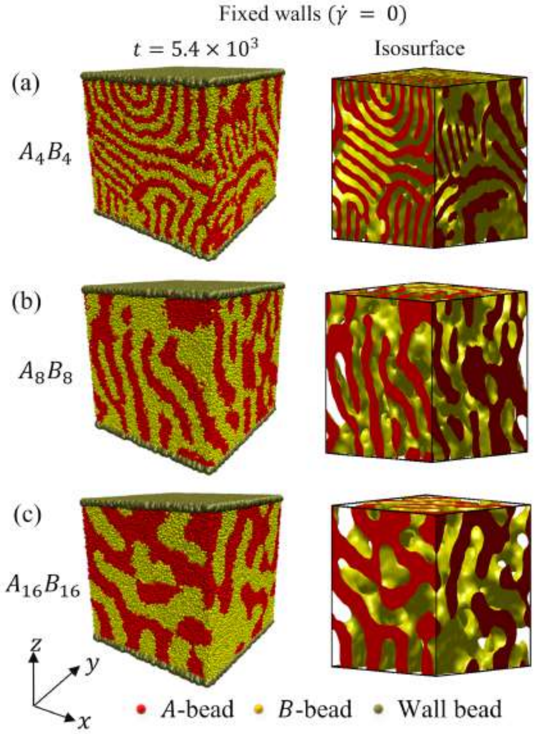

Fig. 4.5: Comparison of late stage morphology of phase separating critical BCP melt for (a) $N_p = 8$, (b) $N_p = 16$, and (c) $N_p = 32$. The second right frame shows the corresponding isosurfaces.

First, we examine the scenario with zero shear effect when both walls are stationary. This serves as the reference case to maintain the rest of the discussion in the proper context. We have illustrated the domain morphologies at a late time, $t = 5.4 \times 10^3$, for three different chain lengths: $N_p = 8$, 16, and 32 in Figs. 4.5(a), 4.5(b), and 4.5(c), respectively. The red color indicates the A-type beads, the yellow represents the B-type beads, and the olive color denotes the wall beads. We have plotted the evolution for different chain lengths to compare the time needed to achieve lamellar structures, typically observed in all symmetric block copolymer (BCP) melt systems. From the mathematical expression of the diffusion coefficient, $D \sim N_p^{-\nu}$, where $\nu = 1/2$, it is evident that lamellar structures can be attained more quickly in symmetric BCP melts with shorter chain lengths. By comparing the evolution snapshots shown in Figs. 4.5(a), 4.5(b), and 4.5(c), distinct lamellar morphology is observed for $N_p = 8$ (A_4B_4) and $N_p = 16$ (A_8B_8), while longer time steps are required for $N_p = 32$ ($A_{16}B_{16}$).

4.7.1 RDF and density distribution

To quantify the domain evolution for the chain length $N_p = 32$, we plot the radial distribution function (RDF), $g_{AB}(r)$, vs. radial distance, r, in Fig. 4.6(a) for case 1, where both walls are stationary. The data is plotted at different time steps and represented by various symbols in the legend. The black curve, plotted at an early time ($t = 1.2 \times 10^2$), has a lower peak at a smaller r value and saturates later. This indicates the formation of smaller microdomains at early times. At later time intervals, shown by the red ($t = 3.6 \times 10^2$), green ($t = 1.2 \times 10^3$), and blue ($t = 5.4 \times 10^3$) curves, the RDF curves start developing secondary peaks, indicating the evolution into periodic domains. As time progresses, the shifting of peaks towards higher r values and the increase in peak heights represent the growth of separate A and B clusters. Furthermore, the local number density of A-type beads is plotted in Fig. 4.6(b) along the y-direction for the same time intervals as in Fig. 4.6(a). The solid line represents the actual value of $\rho_A = 1.453$. The increasing peak height and oscillation of the density profile curves indicate the formation of periodic structures over time. Due to brevity, the density profile is displayed only in one direction.

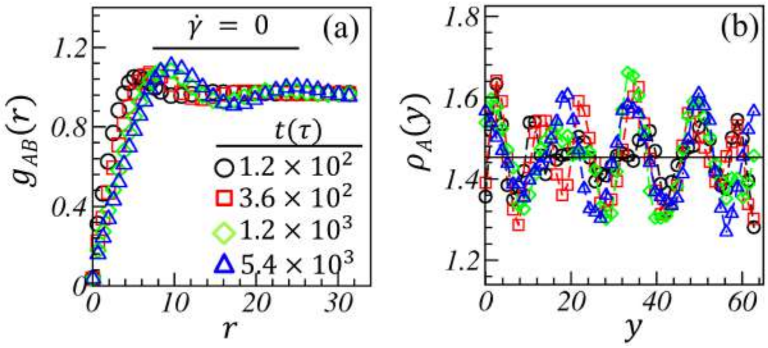

Fig. 4.6: (a) Plots for the radial distribution function $g_{AB}(r)$ vs. r for BCP chain length $N_p = 32$ for case 1. Different symbols types mentioned in the legends represent the various time intervals. (b) Average number density distribution function $\rho_A(y)$ vs. y of A-type beads, corresponding to the same time intervals as in (a).

4.7.2 Characterization functions

To characterize the domain evolution, we plot the spherically averaged scaled correlation function and the corresponding structure factor in Figs. 4.7(a) and 4.7(b), respectively, at different time intervals. Since the early-time evolution in BCP melts is similar to the spinodal decomposition in polymer blends [67], we notice a slight deviation from the scaling behavior in the black ($t = 1.2 \times 10^2$) and red ($t = 3.6 \times 10^2$) curves. Conversely, in the green ($t = 1.2 \times 10^3$) and blue (5.4×10^3) curves, there is an excellent overlap in the data, indicating the dynamical scaling regime. As time progresses, the development of periodic domains is observed. This is evidenced by oscillations in the correlation curves after crossing zero at later time intervals. The corresponding scaled structure factor $S(k,t)R(t)^{-3}$ vs. $kR(t)$ is shown in Fig. 4.7(b). As discussed with the correlation function data, a small deviation is observed in the early-time structure factor, represented by the black and red symbols. Corresponding to the late-time morphology, the prominent peaks of the structure factor become sharper, and a distinct shoulder also appears in the green ($t = 1.2 \times 10^3$) and blue ($t = 5.4 \times 10^3$) curves. This verifies the formation of periodic structures at late time intervals. The tails of the structure factor follow Porod's law, $S(k,t) \sim k^{-(d+1)}$, in the large wave vector ($k \to \infty$) regimes, which results from scattering off sharp interfaces [27].

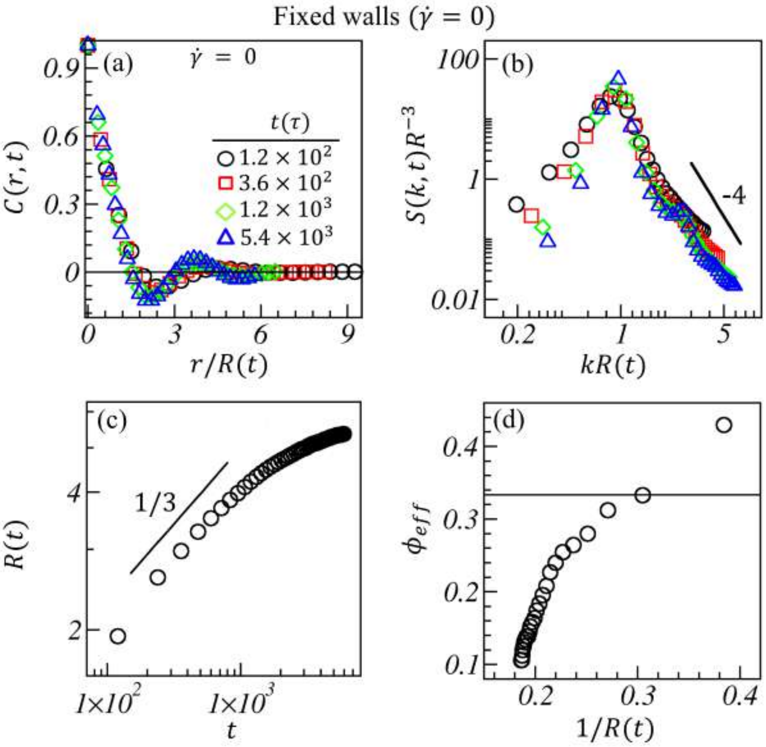

Fig. 4.7: (a-b) Spherically averaged scaled correlation $C(r,t)$ vs. $r/R(t)$ and corresponding structure factor $S(k,t)$ vs. $kR(t)$ are plotted for different time intervals with various symbols mentioned in the legends. The solid black line in (a) represents the zero crossing of correlation function. The structure factor curves follow Porod's law: $S(k,t) \sim k^{-4}$ at $k \to \infty$ represented by a solid black line with slope -4. (c) The characteristic length scale over time for case 1. The solid black line with slope 1/3 represents the diffusive growth at early times which saturates later. (d) Plots for the effective growth exponent ϕ_{eff} vs. $1/R(t)$ correspond to the length scale plotted in (c). The solid black line illustrates the reference value of $\phi_{eff} \sim 1/3$ for early diffusive growth.

In Fig. 4.7(c), we plot the characteristic length scale $R(t)$ vs. t corresponding to the evolution shown in Fig. 4.5(c). During the early spinodal time window, up to $t_{sp} \simeq 2.0 \times 10^3$, the length scale follows diffusive growth with $R(t_{sp}) \sim 6$, which is equivalent to the average size of BCP sub-chains. At later time intervals, when the bond constraints between the BCP sub-chains become significant, the length scale transitions to saturation, resulting in frozen morphologies. Further, we compute the growth exponent from Eq. (1.32), and plot ϕ_{eff} vs. $R(t)^{-1}$ in Fig 4.7(d). At smaller domain sizes, the growth exponent has values near $\phi_{eff} \sim 1/3$, representing diffusive growth, but as $R(t)^{-1} \to 0$, the growth exponent converges to $\phi_{eff} \to 0$, illustrating the saturation at the late time intervals.

4.8 Case 2: Only top wall moves

Now, we focus on the phase separation of BCP melts under the effect of external shear. We start with case 2, where only the top walls are allowed to move in positive x-direction, and the bottom walls remain stationary. We have given three different velocities to the top wall and consequently three different shear rates $\dot{\gamma} = 1.56 \times 10^{-3}$, 7.80×10^{-3}, and 1.56×10^{-2} are applied to the system.

We compare the domain evolution at different shear rates for case 2 in Fig. 4.8. Due to the motion of the top wall, the A and B type domains adjacent to the top wall start flowing in the direction of the shear. As we increase the shear rate, the effect of wall motion intensifies, and the domains attempt to reorient themselves along the shear direction to minimize its impact. Recall that we could not attain the lamellar morphology in case 1 up to our simulation time of $t = 5.4 \times 10^3$. However, in this case, the lamellar sheets develop earlier with an increasing shear rate. As a consequence of the competition between the shear effect and the phase separation kinetics, the A and B sub-chains segregate perpendicular to the shear direction to attain a more stable lamellar structure. As only the top wall is moving, only a small region near the top wall is influenced at a low shear rate of $\dot{\gamma} = 1.56 \times 10^{-3}$. Thus, we notice the formation of lamellar structures close to the top wall along the flow direction and perpendicular to the yz-plane. However, as we increase the shear rate to $\dot{\gamma} = 7.80 \times 10^{-3}$ and $\dot{\gamma} = 1.56 \times 10^{-2}$, more layers of the

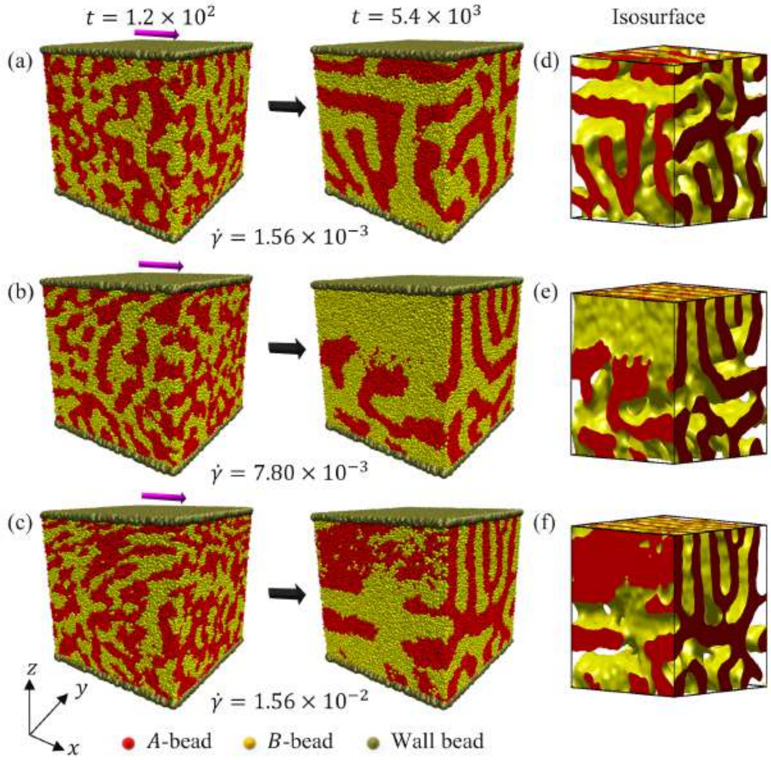

Fig. 4.8: Morphology evolution of BCP melts system for case 2 for three different shear rates (a) $\dot{\gamma} = 1.56 \times 10^{-3}$, (b) $\dot{\gamma} = 7.80 \times 10^{-3}$, and (c) $\dot{\gamma} = 1.56 \times 10^{-2}$. The snapshots are taken at two different time intervals: $t = 1.2 \times 10^2$ (first column) and $t = 5.4 \times 10^3$ (second column). The direction of the wall motion is shown with a magenta arrow. In the third column, the isosurfaces are plotted, corresponding to the evolution shown in the second column.

simulation box are affected by the moving wall. Consequently, more ordered lamellar sheets form at high shear rates after the same time interval. Applying unidirectional shear increases the tendency to form well-ordered structures, such as lamellae in our case of symmetric BCP melt.

4.8.1 RDF and density distribution

In Fig. 4.9(a), we plot the radial distribution function $g_{AB}(r)$ vs. r corresponding to the morphology shown in Fig. 4.8. Various symbol types represent different time intervals at a fixed shear rate of $\dot{\gamma} = 7.80 \times 10^{-3}$. In the black curve, plotted at the early time $t = 1.2 \times 10^2$, a single peak is observed at a smaller r value, $r \simeq 5.0$, indicating the formation of tiny microdomains at early times. The strength of the primary peak increases with time, and its position shifts towards higher distances, reaching $r \simeq 9.25$ in the blue curve. At later times, a secondary peak is clearly visible in the blue curve at $r \simeq 24.0$, representing the formation of the lamellar structure. Corresponding to the data shown in Fig. 4.9(a), we plot the local number density distribution of A-type particles along the y-direction in Fig. 4.9(b). At early times, a smaller amplitude is noted in the density profile, verifying the formation of tiny microdomains. However, a more significant amplitude and oscillation are observed at later time intervals, illustrating the formation of larger and periodic domains.

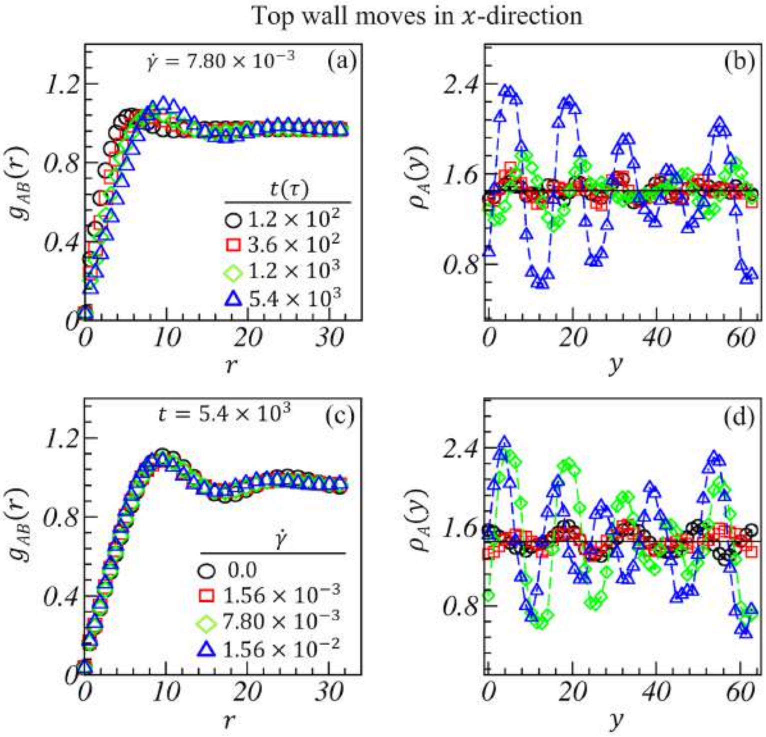

Fig. 4.9: (a) and (b) represents the plots of $g_{AB}(r)$ vs. r and $\rho(y)$ of A-beads along y-direction, respectively for case 2. These data sets are computed at a fixed shear rate of $\dot{\gamma} = 7.80 \times 10^{-3}$ for different time intervals mentioned in the legends. (c) $g_{AB}(r)$ vs. r for different shear rates at a fixed time interval of $t = 5.4 \times 10^3$. (d) $\rho(y)$ versus y for the same data set as in (c).

Further, we compare $g_{AB}(r)$ vs. r for different shear rates in Fig. 4.9(c) at a late time interval $t = 5.4 \times 10^3$. An excellent overlap is noted in the RDF data near the first peak. However, the prominent peak becomes sharper at high shear rates, and its position also shifts towards smaller distances, specifically at $r \simeq 9.6$, 9.6, 9.25, and 9.0. At different $\dot{\gamma}$ values, the formation of a secondary peak represents the periodic structures. With an increase in shear rate, specifically at $\dot{\gamma} = 0.0$, 1.56×10^{-3}, 7.80×10^{-3}, and 1.56×10^{-2}, the position of the secondary peaks also shifts left to $r \simeq 25.0$, 24.32, 24.0, and 22.4, respectively. These outcomes suggest the formation of periodic morphology and the thinning of the domains at high shear rates. In Fig. 4.9(d), we plot the local number density profile for different shear rates, as indicated in the legends. At smaller $\dot{\gamma}$ values, the lower amplitudes in the black and red curves imply that fully developed lamellae stripes are not yet formed, and many small, randomly oriented stripes remain in the system. In contrast, at high shear rates ($\dot{\gamma} = 7.80 \times 10^{-3}$ and 1.56×10^{-2}), the density profiles show higher and more periodic peaks, suggesting the formation of a well-developed lamellar morphology.

4.8.2 Characterization functions

To characterize the domain evolution at different shear rates for case 2, we plot the spherically averaged scale correlation function $C(r, t)$ vs. $r/R(t)$ in Fig. 4.10(a) and $S(k, t)$ vs. $kR(t)$ on logarithmic scale in Fig. 4.10(b). Different symbols represent the various shear rates applied to the system. The oscillatory nature of the correlation function and the appearance of a distinct shoulder in the structure factor curves indicate the development of periodic morphology at later times. Notice that for $\dot{\gamma} \neq 0.0$, the amplitude of oscillation in correlation function decreases, and the prominent peak of $S(k, t)$ broadens. Since the average domain size is defined as the inverse of the first moment of the structure factor ($\langle k \rangle \sim R(t)^{-1}$) [1,6], the broadening of the prominent peaks confirms shear thinning at later times. The distinct shoulder in the structure factor shifts towards higher $kR(t)$-values with the application of shear. It is positioned at $kR(t) \simeq 2.67$ for $\dot{\gamma} = 0.0$ (black curve), whereas it moves to a larger $kR(t) \simeq 3.06$ in the blue curve. These results also indicate shear-thinning morphologies. There is excellent overlap in the scaling function curves shown in Figs. 4.10(a)-4.10(b) for $\dot{\gamma} \neq 0.0$, with a slight deviation noted in the black curve ($\dot{\gamma} = 0.0$). Thus, the scaling functions belong to the same universality class under shear. For all cases, the structure factor follows Porod's law, shown as a solid black line with a slope of -4.

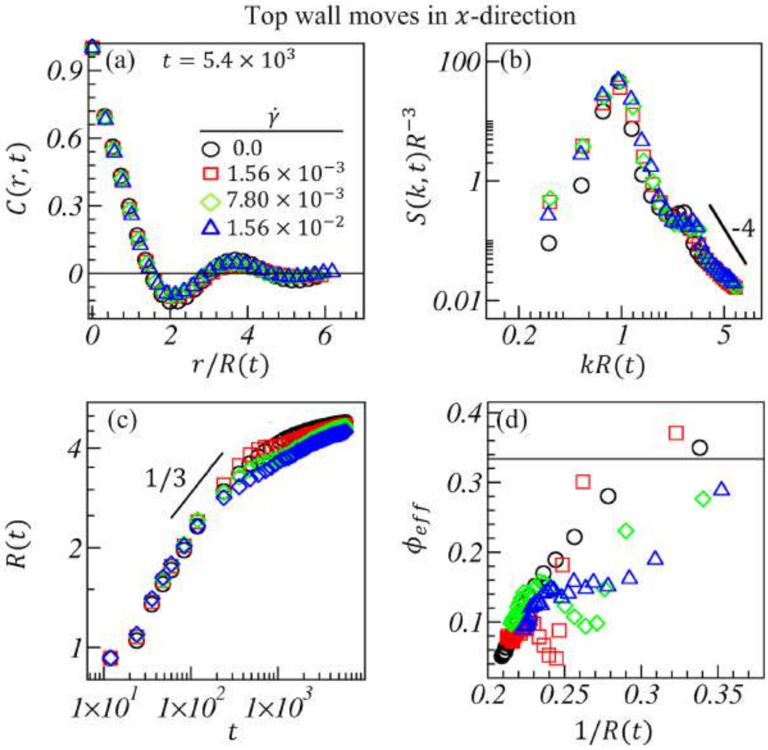

Fig. 4.10: The characterization functions are plotted at a fixed time step $t = 5.4 \times 10^3$ for different shear rates for case 2. The scaled correlation function $C(r,t)$ versus $r/R(t)$ is displayed in (a), While the corresponding structure factor $S(k,t)$ versus $kR(t)$ on a logarithmic scale is shown in (b). (c) The characteristic length scale is plotted against time for given shear rates. To calculate the growth exponent, we display the ϕ_{eff} as a function of $1/R(t)$ in (d).

Further, we compare $R(t)$ vs. t on a log-log scale in Fig. 4.10(c) and the corresponding ϕ_{eff} in Fig. 4.10(d) for different shear rates. The black curve is plotted for case 1 as a reference. Two processes occur simultaneously: domain coarsening and the flow of domains along the shear direction. At a low shear rate of $\dot{\gamma} = 1.56 \times 10^{-3}$ (red curve), domain coarsening is dominant, following early-time diffusive growth ($R(t) \sim t^{1/3}$). Consequently, a larger average domain size is observed up to $t_{sp} \simeq 6.0 \times 10^{2}$, indicating lower shear thinning than other curves at higher $\dot{\gamma}$ values. At late times ($t > t_{sp}$), topological constraints become significant. We observe a dip in the length scale curves for a certain duration ($6.0 \times 10^{2} < t < 1.0 \times 10^{3}$) as the A and B type domains adjust to a more stable arrangement along the shear direction. After this period, the length scale grows and eventually reaches saturation, indicating frozen structures at smaller $R(t)$ values. This behavior reflects the shear-thinning effect in the system. As shear rates increase, the effect of shear becomes more prominent, causing domain thinning at early times. This results in a decreased overall growth rate. From the growth exponents, we notice values near the diffusive growth regime in the early times, which then transition to saturation, leading to the formation of frozen morphology later. In Fig. 4.10(d), we plot ϕ_{eff} vs. $1/R(t)$, which illustrates the same behavior: $\phi_{eff} \to 0$ as $1/R(t) \to 0$.

4.9 Case 3: Both walls move in the same direction

Now, we move to case 3, where the top and bottom walls move with the same velocity along the x-direction. We monitor the domain evolution for different shear rates in Fig. 4.11 at two different time intervals, $t = 1.2 \times 10^{2}$ and $t = 5.4 \times 10^{3}$, shown in the first and second columns, respectively. In this case, shear is applied from both directions, and its effect is more pronounced at high shear rates, ranging from $\dot{\gamma} = 7.80 \times 10^{-3}$ to 1.56×10^{-2}. Due to the effect of moving walls, periodic structures start developing from the top and bottom walls, with the effect being more prominent closer to the walls than in other areas. At the same shear rates, we notice a more explicit formation of lamellar morphology in this case compared to case 2. At the low shear rate of $\dot{\gamma} = 1.56 \times 10^{-3}$, the effect of wall motion on the evolution is similar in cases 2 and 3.

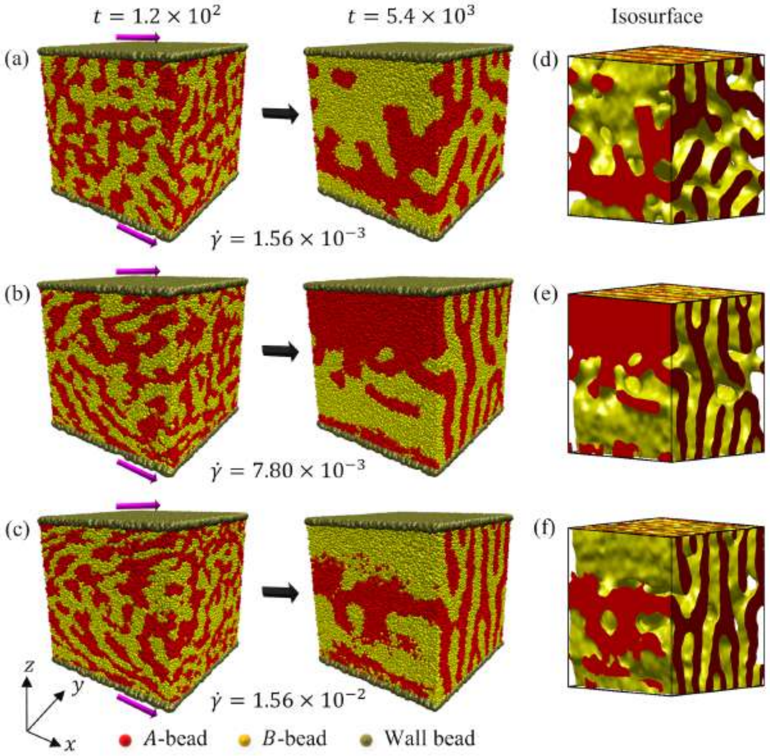

Fig. 4.11: The evolution snapshots for case 3, where both walls move in the same direction. Snapshots are plotted at two-time steps $t = 1.2 \times 10^2$ and $t = 5.4 \times 10^3$. The shear rates applied to the system is varied as: (a) $\dot{\gamma} = 1.56 \times 10^{-3}$, (b) $\dot{\gamma} = 7.80 \times 10^{-3}$, and (c) $\dot{\gamma} = 1.56 \times 10^{-2}$. The third column represents the isosurfaces corresponding to the snapshots in the second column. The magenta arrows display the shear direction.

4.9.1 RDF and density distribution

We plot the radial distribution function $g_{AB}(r)$ vs. r in Fig. 4.12(a) at the later time interval $t = 5.4 \times 10^3$. Different symbols indicate the various shear rates as per the legend. As previously discussed, higher shear rates result in increased oscillations in the RDF curves, indicating greater periodicity. The peak positions also shift to smaller distances; the primary peaks occur at $r \simeq 9.6$, 9.5, 9.0, 9.0, and the secondary peaks at $r \simeq 25.0$, 24.32, 23.04, 22.4, respectively. This confirms that domain thinning occurs with

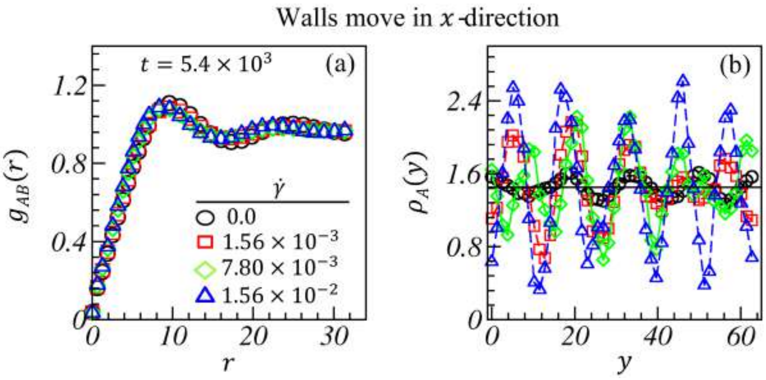

Fig. 4.12: Case 3: Both walls are moving in x-direction with similar velocities. (a) Plots the $g_{AB}(r)$ versus r, and (b) the average number density profiles of A-type beads in y-direction at $t = 5.4 \times 10^3$ for different shear rates; related morphologies are shown in Fig. (4.11)

increasing shear rates. In Fig. 4.12(b), we observe the local number density distribution of A-type beads along the y-direction. The curves depict symmetric density profiles around the average value ($\rho_A = 1.453$). A comparison with the previous case reveals an increased amplitude of $\rho_A(y)$, indicating the formation of well-defined lamellar structures. Notably, the green and blue curves at $\dot{\gamma} = 7.80 \times 10^{-3}$ and $\dot{\gamma} = 1.56 \times 10^{-2}$ respectively exhibit enhanced amplitudes, signifying pronounced lamellar structure formation. At a low shear rate of $\dot{\gamma} = 1.56 \times 10^{-3}$, the red curve demonstrates a noticeable density peak enhancement compared to the previous case, suggesting that more ordered structures are formed in this scenario at the same shear rates.

4.9.2 Characterization functions

The scaling functions for late-time evolution are depicted in Figs. 4.13(a) ($C(r,t)$ vs. $r/R(t)$) and 4.13(b) ($S(k,t)$ vs. $kR(t)$) for various shear rates. Related snapshots are in Fig. 4.11. The correlation and structure factor curves at a low shear rate $\dot{\gamma} = 1.56 \times 10^{-3}$ show a divergence from the reference black curve. Similarly, the green and blue curves at high shear rates exhibit a slight deviation from the reference. However, $C(r,t)$ and $S(k,t)$ data at high shear rates align perfectly, demonstrating dynamic scaling. The structure factor curves adhere to Porod's law across different shear rates, indicating sharp domain interfaces between A and B beads. The formation of periodic structures under shear is evidenced by oscillations in the correlation function and distinct secondary peaks in the structure factor curves. At high shear rates, the oscillation amplitude in the correlation function decreases after the zero crossing, and there is a broadening of the prominent peaks in the structure factor. These results indicate the shear thinning of evolving morphologies.

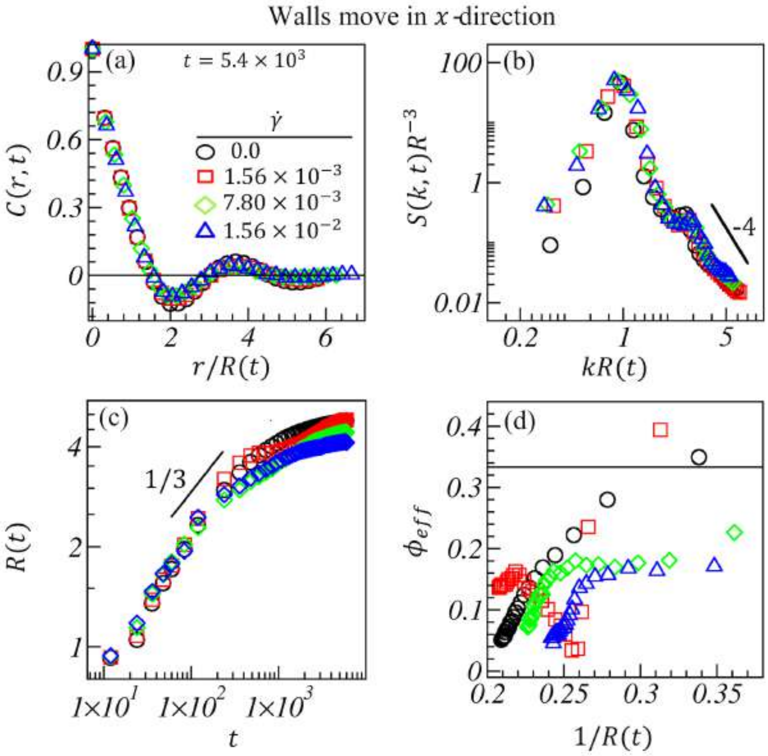

Fig. 4.13: (a) Spherically averaged $C(r,t)$ vs. $r/R(t)$ for different shear rates; related morphologies are illustrated in Fig. 4.11. The corresponding $S(k,t)$ versus $kR(t)$ curves are plotted in (b) on a log-log scale. (c) $R(t)$ versus t for different sher rates. (d) Plots for related effective growth exponents ϕ_{eff} versus $1/R(t)$.

Additionally, we compare the characteristic average domain growth $R(t)$ vs. t in Fig. 4.13(c) for different shear rates. At a low shear rate, early-time diffusive growth is supported, leading to larger domain sizes up to $t_{sp} \simeq 6.0 \times 10^2$ (red curve). Subsequently, up to $t \simeq 1.0 \times 10^3$, domain growth is minimal due to the competing effects of phase separation and shear. This period shows a noticeable dip in the growth exponent (see red curve in Fig. 4.13(d)). During this time, the BCP chains locally rearrange to minimize the impact of shear.

Afterward, domains resume growth at a reduced rate due to shear thinning compared to case 1. However, the length scale eventually saturates at a slightly larger value than the reference case (see red curves in Figs. 4.13(c) and 4.13(d)). At higher shear rates, $\dot{\gamma} = 7.80 \times 10^{-3}$ (green curve) and $\dot{\gamma} = 1.56 \times 10^{-2}$ (blue curve), the shear effect is significant from the outset, resulting in a smaller early-time growth exponent ($\phi_{eff} \simeq 0.2$). The length scale later saturates with smaller domain sizes, further indicating shear thinning. Therefore, shear thinning is more pronounced at higher shear rates. The growth exponent analysis shows that as $R(t)^{-1} \to 0$, the growth exponent $\phi_{eff} \to 0$.

4.9.3 Anisotropy developed in case 2 and case 3

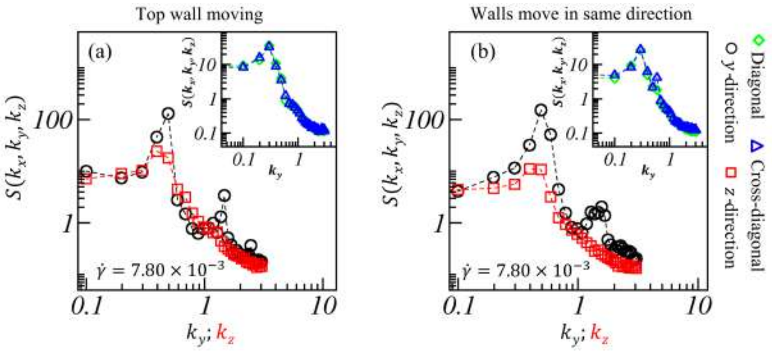

Fig. 4.14: Plots for the unidirectional structure factor $S(k_x, k_y, k_z)$ versus k_y (black curve) and k_z (red curve) to discuss the structural anisotropy in the system. The data is calculated at a fixed shear rate of $\dot{\gamma} = 7.80 \times 10^{-3}$ and plotted for case 2 in (a) while for case 3 in (b). The inset represents the $S(k_x, k_y, k_z)$ versus k_y along diagonal and cross-diagonal directions with green and blue curves, respectively, in yz-plane.

Recall that we have plotted the spherically averaged correlation and structure factor. The critical BCP melt tends to form a lamellar structure in the asymptotic limit, making it interesting to examine the structural anisotropy developed in the system. Therefore, we have plotted the unidirectional structure factor $S(k_x, k_y, k_z)$ in Fig. 4.14 against the wave vector k_y (black curve) and k_z (red curve). Here, $S(k_x, k_y, k_z)$ is plotted at a fixed shear rate of $\dot{\gamma} = 7.80 \times 10^{-3}$ at $t = 5.4 \times 10^3$ for case 2 in (a) and case 3 in (b). We observe sharper peaks with high amplitude in the black curve along the direction perpendicular to the lamellae sheet (k_y-direction). Meanwhile, the red curve plotted along k_z (parallel to the lamellar strips) exhibits a single peak with lower amplitude. These curves along different directions demonstrate the structural anisotropy developed in cases 2 and 3. Comparing the black curves in Figs. 4.14(a) and 4.14(b), the higher amplitude of the peaks in Fig. 4.14(b) indicates more significant anisotropy in case 3 compared to case 2. Since the lamellar slabs form along the xz-plane, the variation of $S(k_x, k_y, k_z)$ along k_x and k_z directions is similar (parallel to the slabs). Therefore, we have not shown the structure factor comparison along these directions for brevity. The insets in both figures show $S(k_x, k_y, k_z)$ vs. k_y along diagonal and cross-diagonal directions with green and blue curves, respectively. The excellent overlap in these data confirms the symmetric arrangement of the lamellar sheets in the yz-plane.

4.10 Case 4: Both walls move in opposite directions

In this case, both walls move in opposite directions with the same velocity: the top wall moves along the positive x-direction, while the bottom wall moves in the negative x-direction. In Fig. 4.15, we plot the evolution snapshots for different shear rates and the corresponding isosurfaces. We observe the formation of lamellar morphology much earlier compared to cases 1-3. This may be due to the opposite direction of applied shear, facilitating a more rapid readjustment of the domains. At high shear rates, $\dot{\gamma} = 7.80 \times 10^{-3}$ and $\dot{\gamma} = 1.56 \times 10^{-2}$, well-ordered lamellar patterns are formed after the same time intervals. However, at a low shear rate, $\dot{\gamma} = 1.56 \times 10^{-3}$, a few shorter A and B patches are formed, which are elongated along the x-direction.

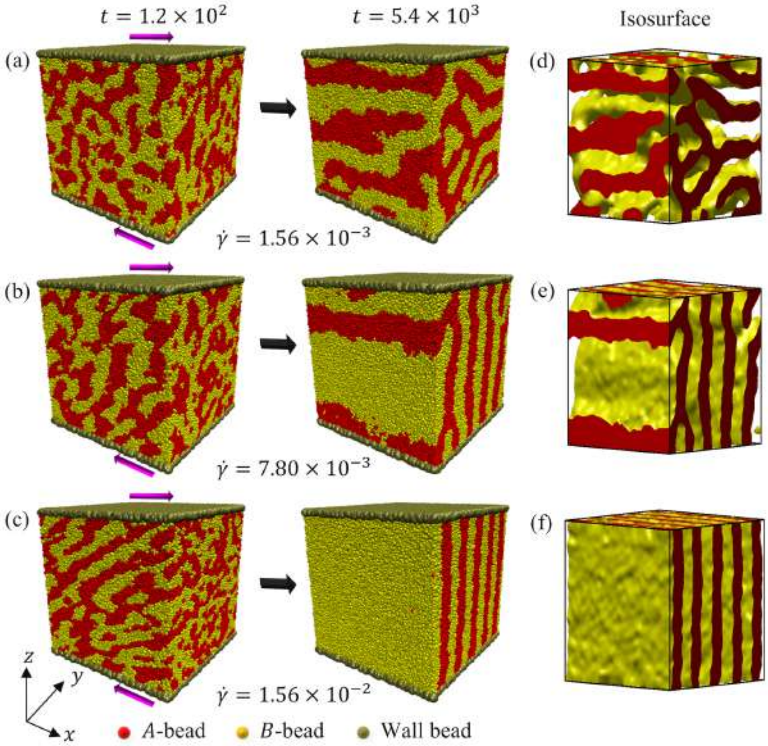

Fig. 4.15: Case 4: The evolution snapshots at two different time steps $t = 1.2 \times 10^2$ and $t = 5.4 \times 10^3$ for different shear rates (a) $\dot{\gamma} = 1.56 \times 10^{-3}$, (b) $\dot{\gamma} = 7.80 \times 10^{-3}$, and (c) $\dot{\gamma} = 1.56 \times 10^{-2}$. To see the bulk structures, we have plotted the isosurfaces in column three corresponding to the snapshots at $t = 5.4 \times 10^3$.

4.10.1 Characterization of domain coarsening

As discussed in previous cases, the plots for the radial distribution function (RDF) shown in Fig. 4.16(a) exhibit similar late-time behavior for all shear rates $\dot{\gamma}$. With an increase in shear rate, more ordered and periodic lamellar structures form, as evidenced by the more oscillatory and sharper RDF peaks at high shear rates. The shift in RDF peaks towards lower r values, such as primary peaks at $r \simeq 9.5$, 9.0, 8.32 and secondary peaks at $r \simeq 24.96$, 22.40, 21.76 in the red, green, and blue curves, respectively, indicates the shear thinning of the domains with increasing shear rate. Corresponding to these data, we plot the density profile of A-type beads along the y-direction in Fig. 4.16(b). At high shear rates, the increase in amplitude and sharpness of the peaks represents the formation of well-separated A and B type clusters. In the green and blue curves in Fig.

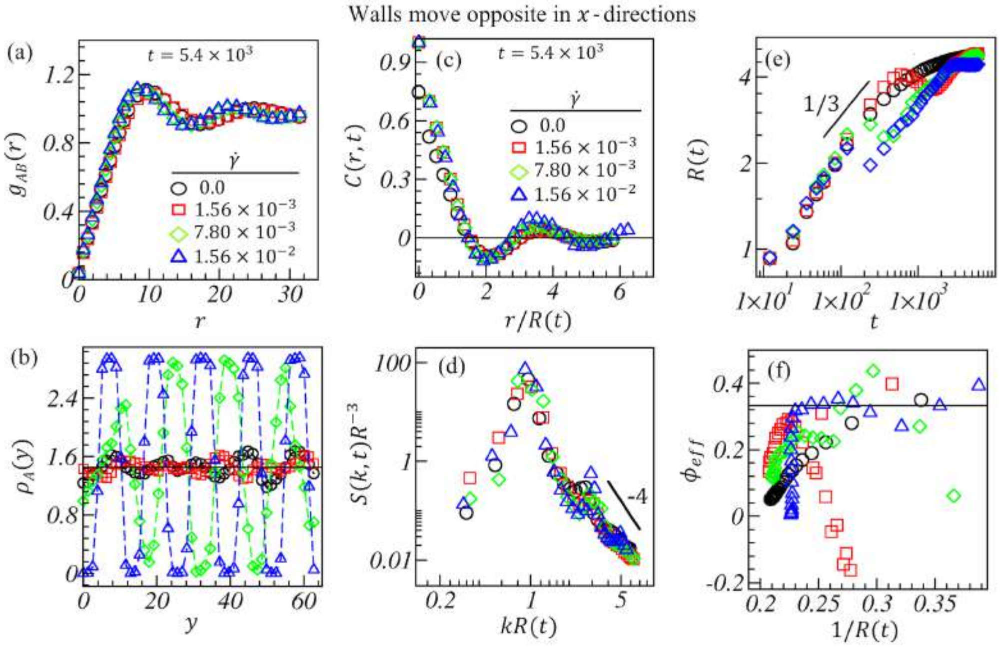

Fig. 4.16: Case 4: (a) Comparison of $g_{AB}(r)$ versus r, (b) $\rho(y)$ versus y of A-type beads, (c) $C(r,t)$ versus $r/R(t)$, and (d) $S(k,t)$ versus $kR(t)$ at $t = 5.4 \times 10^3$ for different shear rates mentioned in the legends. (e) The characteristic average domain size $R(t)$ vs. t for the evolution displayed in Fig. 4.15. (f) Plots for the effective growth exponents ϕ_{eff} vs. $1/R(t)$ for different shear rates.

4.16(b), plotted at $\dot{\gamma} = 7.80 \times 10^{-3}$ and $\dot{\gamma} = 1.56 \times 10^{-2}$, the density profile peaks have nearly equal periodicity and amplitude, manifesting the formation of lamellar morphology normal to the y-direction.

To characterize the evolved morphology, we plot the scaled correlation function $C(r,t)$ vs. $r/R(t)$ in Fig. 4.16(c) and the corresponding structure factor $S(k,t)$ vs. $kR(t)$ in Fig. 4.16(d). In case 4, a notable deviation from the scaling behavior is observed. In cases 2 and 3, scaling was evident in the correlation at lower r values and the structure factor at higher k values. Furthermore, increased oscillation is noted in the correlation functions at high shear rates. In the structure factor data, a distinct shoulder appears at $kR(t) \simeq 2.67$, 2.84, 2.86, and 2.93 for $\dot{\gamma} = 0.0$, 1.56×10^{-3}, 7.80×10^{-3}, and 1.56×10^{-2}, respectively. At high shear rates, $\dot{\gamma} = 7.80 \times 10^{-3}$ and 1.56×10^{-2}, the development of another shoulder is also noted at higher $kR(t)$ values of $kR(t) \simeq 4.68$ and 4.95, respectively. These results justify the formation of well-developed lamellar morphology in this case compared to cases 2 and 3, particularly at $t = 5.4 \times 10^3$ for $\dot{\gamma} = 1.56 \times 10^{-2}$.

The characteristic length scale corresponding to the evolution shown in Fig. 4.15 is compared in Fig. 4.16(e) for different shear rates mentioned in the legends. The corresponding growth exponents are also plotted in Fig. 4.16(f). For reference, the black curve is plotted at a zero shear rate. At a low shear rate of $\dot{\gamma} = 1.56 \times 10^{-3}$ (red curve), the length scale follows the diffusive growth $\phi \to 1/3$ up to $t_{sp} \simeq 6.0 \times 10^2$ and deviates afterward. At the time step $t \simeq 1.4 \times 10^3$ (see the red curve in Figs. 4.16(e)-4.16(f)), a dip in the length scale curve is noted due to the competition between the shear effect and domain coarsening. The shear effect starts dominating over diffusion, causing the BCP chains to rearrange perpendicular to the shear direction to minimize its impact, leading to the dip in the length scale curve during this period. A similar dip is also noted in the green ($\dot{\gamma} = 7.80 \times 10^{-3}$) and the blue ($\dot{\gamma} = 1.56 \times 10^{-2}$) curves at earlier times compared to the red curve. After the dip, the length scale starts growing at all shear rates and follows diffusive growth for a more extended period before saturation. At the high shear rate of $\dot{\gamma} = 1.56 \times 10^{-2}$, the saturation length is smaller compared to lower $\dot{\gamma}$ values, justifying the shear thinning of the domains as shown in Fig. 4.15(c). However, the green and blue curves saturate at the same $R(t)$ value as the reference black curve. The effective growth exponent represents the saturation of the length scale in the asymptotic limit. Overall, the effect of moving parallel walls is more significant in case 4, resulting in the formation of lamellar morphology much earlier in the microphase separating critical BCP melts.

Domain coarsening in the critical BCP melt system is a well-known phenomenon. Initially, domain evolution in this system follows diffusive growth ($R(t) \sim t^{1/3}$), eventually leading to frozen lamellar structures at later stages [95]. For instance, under zero shear, it takes a long time, around $t \approx 2 \times 10^4$, to achieve lamellar morphology for a chain length $N_p = 32$ and system size $64 \times 64 \times 64$. However, applying a high shear rate ($\dot{\gamma} = 1.56 \times 10^{-2}$) in case 4 significantly reduces the time to approximately $t \approx 5 \times 10^3$ to form lamellar morphology for the same system size. Therefore, we investigate phase separation kinetics under different conditions to highlight the impact of shear on the resulting morphology.

4.10.2 Anisotropy for different shear rates

Here, we plot the unidirectional structure factor $S(k_x, k_y, k_z)$ along different directions. Their non-overlapping behavior indicates the structural anisotropy developed in the system. In Fig. 4.17, we plot $S(k_x, k_y, k_z)$ at the late time $t = 5.4 \times 10^3$ for $\dot{\gamma} = 0.0$, 1.56×10^{-3}, 7.80×10^{-3}, and 1.56×10^{-2}, displayed in (a-d), respectively. The black and red curves represent the variation of the structure factor along k_y and k_z, respectively. At zero shear rate (Fig. 4.17(a)), the black curve shows a slightly higher primary peak than the red curve, with a developing shoulder at higher k_y values. This suggests lamellar morphology may evolve along the k_y direction much later. At a smaller shear rate of $\dot{\gamma} = 1.56 \times 10^{-3}$, A and B stripes are noted in Fig. 4.15(a) nearly parallel to the xy-plane. Consequently, in Fig. 4.17(b), significantly higher peaks are observed in the red curve compared to the black one. At larger k_y and k_z values, an emerging shoulder is apparent in both curves.

From the evolution images in Fig. 4.15, we observe the formation of more distinct lamellar stripes at higher shear rates, oriented normal to the yz-plane and along the x-direction. Consequently, the structure factor along the y-direction (black curve) in Figs. 4.17(c)-4.17(d) shows higher amplitude peaks, indicating the periodic A and B-type stripes formed in this direction. In contrast, the higher-order peaks in the red curve in Fig. 4.17(b) diminish at $\dot{\gamma} = 7.80 \times 10^{-3}$ and 1.56×10^{-2}. This reduction in peaks in the red curve at high shear rates is due to the emergence of more parallel lamellar structures

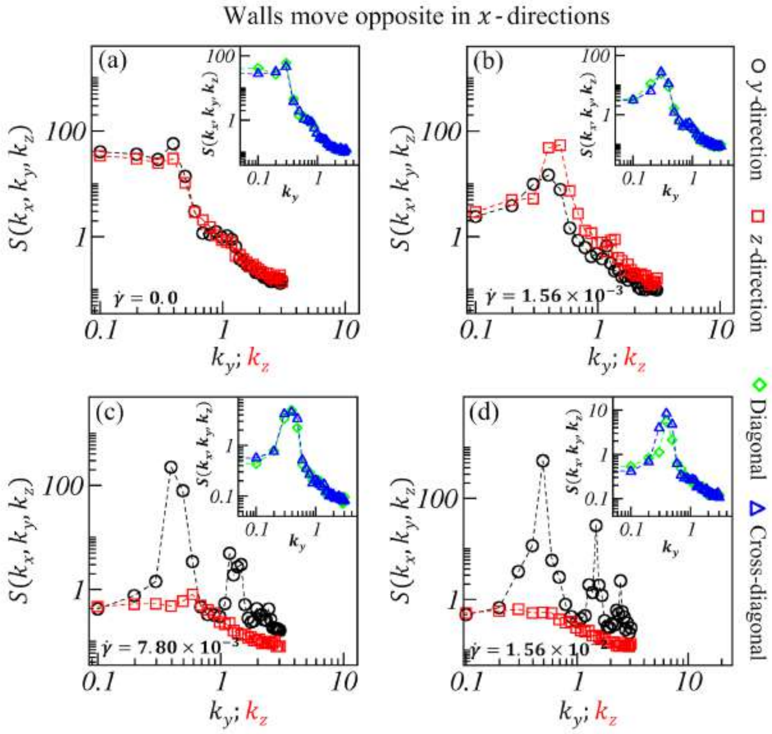

Fig. 4.17: We plot the unidirectional structure factor $S(k_x, k_y, k_z)$ versus k_y (black curve) and k_z (red curve) for different shear rates of $\dot{\gamma} = 0.0$ in (a), $\dot{\gamma} = 1.56 \times 10^{-3}$ in (b), $\dot{\gamma} = 7.80 \times 10^{-3}$ in (c), and $\dot{\gamma} = 1.56 \times 10^{-2}$ in (d) to analyze the structural anisotropy developed in the system.

along the xz-plane. The insets of these figures show the variation of the structure factor along the diagonals in the yz-plane. The excellent data overlap represents the structural symmetry in the yz-plane along the diagonals for all shear rates. With increasing shear, the prominent peaks in the green and blue curves become sharper, and their amplitudes increase, indicating the formation of a more ordered lamellar morphology.

In Fig. 4.18, we plot the anisotropy parameter, $D(t)$, along different planes denoted by various symbols. Typically, BCP melts exhibit inherent anisotropy due to bond constraints in the BCP chains. Consequently, in case 1, the anisotropy parameter has a finite value of $D(t) \sim 0.4$ (see Fig. 4.18(a)). Here, all components, D_{xy}, D_{yz}, and D_{xz}, have approximately the same value, indicating that the BCP melt system has not fully evolved into lamellar morphology within the given time limit of our simulation. In case 2,

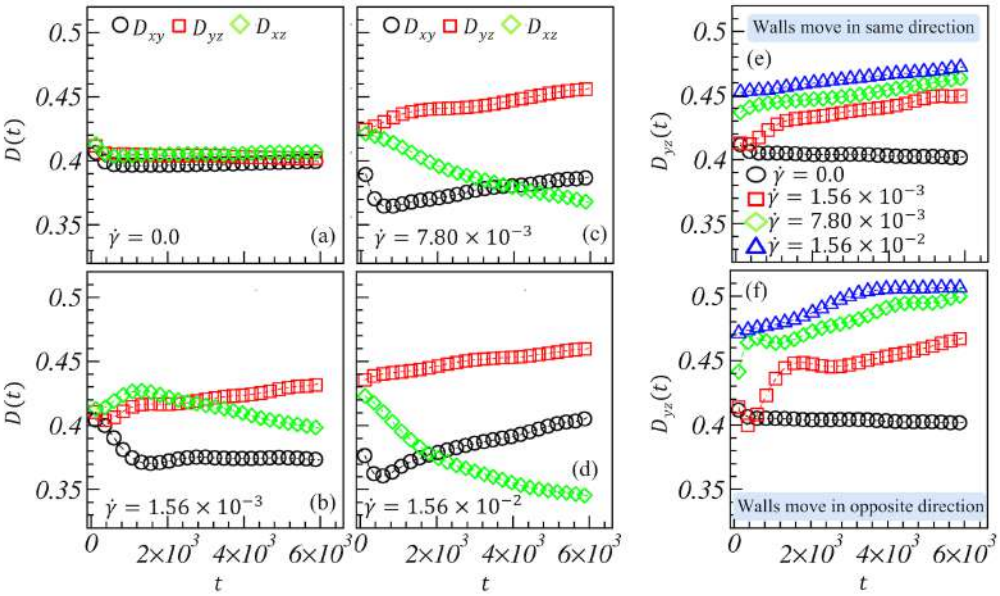

Fig. 4.18: Time variation of anisotropy parameters, D_{xy}, D_{yz}, and D_{xz} are plotted in (a-d). (a) represent the reference case 1 ($\dot{\gamma} = 0.0$). (b-d) plots the same data for case 2 for different shear rates, $\dot{\gamma} = 1.56 \times 10^{-3}$, 7.80×10^{-3}, and 1.56×10^{-2}, respectively. Time variations of D_{yz} are compared in (e) and (f) for case 3 and case 4 at different shear rates depicted by various symbol types.

smaller lamellar microdomains start developing along the xz-plane due to the motion of the top wall along the x-direction (see Fig. 4.8). As a result, the anisotropy parameter decreases along the xz-plane (green curve) and increases along the yz-plane (red curve) over time. The difference in anisotropy becomes more significant later, particularly at high shear rates, due to the formation of distinct lamellar stripes. The developed lamellar structures are aligned along the xz-plane and perpendicular to the yz-plane, leading to an increase in anisotropy along the yz-plane and a decrease along the xz-plane. At a low shear rate of $\dot{\gamma} = 1.56 \times 10^{-3}$, the decrease in the black curve indicates that small microdomains of both phases develop in the xy-plane without specific orientation. However, D_{xy} increases at high shear rates. In Figs. 4.18(e) and 4.18(f), we plot the time variation of D_{yz} for cases 3 and 4, respectively, for different shear rates. In these cases, enhanced anisotropy is noted compared to case 2 due to the application of shear from both directions. Furthermore, as a well-developed lamellar morphology is observed in case 4, the corresponding anisotropy parameter has relatively higher values than in cases 2 and 3 along the yz-plane. The corresponding evolution snapshots are shown in Figs. 4.8, 4.11, and 4.15, respectively.

4.11 BCP melt system with smaller chain length

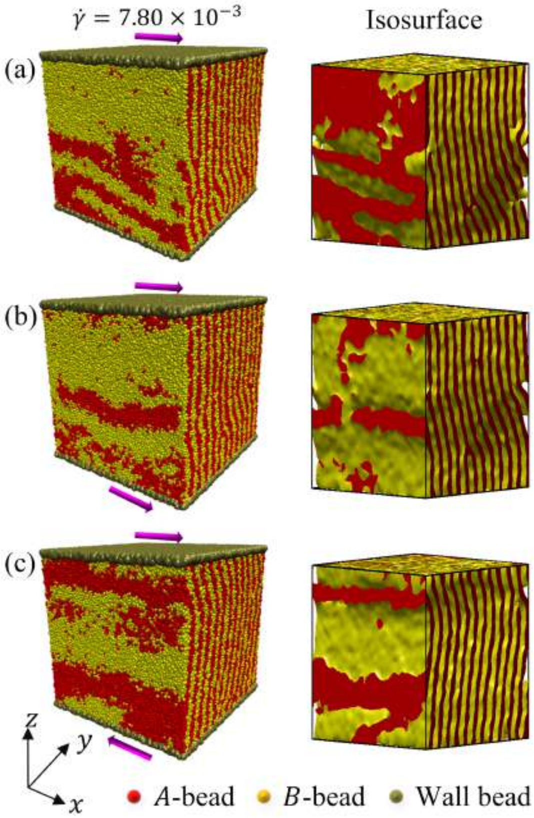

Fig. 4.19: Effect of shear on the BCP melt system with a smaller chain length of A_4B_4. We plot the late time evolution, and related isosurfaces of BCP melt for all three scenarios 2-4 at a fixed moderate shear rate of $\dot{\gamma} = 7.80 \times 10^{-3}$ and time step $t = 5.4 \times 10^3$. Corresponding snapshots for $\dot{\gamma} = 0.0$ is shown in Fig. 4.5(a).

We compare the effect of shear on the critical BCP melt system with smaller chain lengths of $N_p = 8$ and 16. The evolution in these cases without external shear has been discussed previously and shown in Figs. 4.5(a) and 4.5(b). Now, a moderate shear rate of $\dot{\gamma} = 7.80 \times 10^{-3}$ is applied to the system for three different scenarios (2-4) discussed

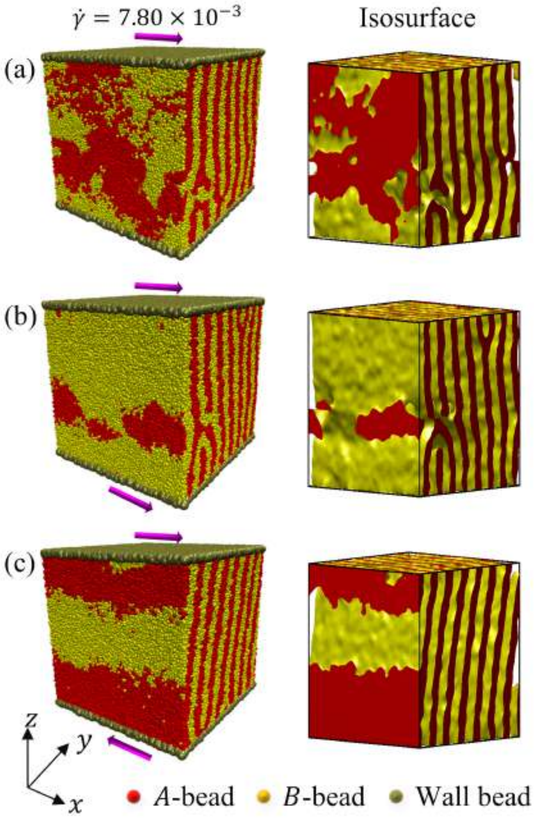

Fig. 4.20: The evolution snapshots and related isosurfaces for a BCP melt system with a smaller chain length of A_8B_8. The shear is applied with cases 2-4 with a moderate shear rate of $\dot{\gamma} = 7.80 \times 10^{-3}$ and time step $t = 5.4 \times 10^3$. Corresponding snapshots for $\dot{\gamma} = 0.0$ is shown in Fig. 4.5(b).

earlier. The evolution at $t = 5.4 \times 10^3$ is plotted for chain lengths of $N_p = 8$ and 16 in Fig. 4.19 and Fig. 4.20, respectively.

As discussed earlier, the diffusion coefficient is defined as $D \sim N_p^{-\nu}$, where $\nu = 1/2$ is the size exponent in the melt [23,172,173]. Due to faster diffusion, lamellar structures form more quickly in symmetric BCP melts with shorter chain lengths. Consequently, lamellar morphologies start developing in Figs. 4.5(a) and 4.5(b) without external shear. Recall that, for a longer chain length of $N_p = 32$, fully developed lamellar structures were observed only in case 4 under the given shear rate and time duration. However, in Fig. 4.19, well-developed lamellar morphologies are achieved in all three scenarios after the same time intervals. In Fig. 4.20, the lamellar structures are also well-developed in all cases, though it takes slightly longer compared to Fig. 4.19. Overall, in symmetric BCP melts with shorter chain lengths, well-ordered lamellar structures form much earlier compared to the results discussed previously with longer BCP chains of $N_p = 32$.

4.12 Effect of shear on asymmetric BCP melt system

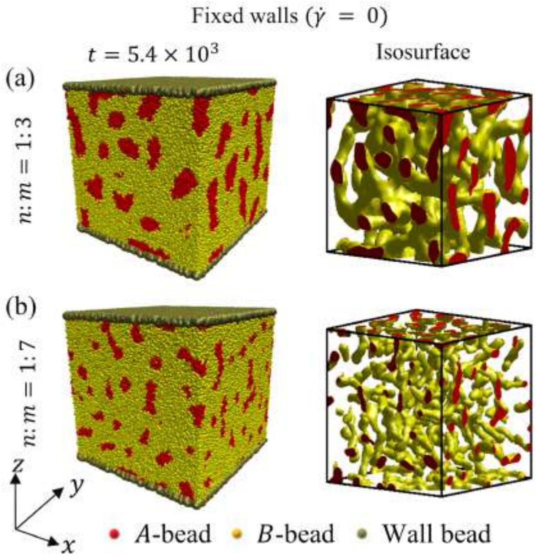

Fig. 4.21: Domain evolution for asymmetric BCP melt system confined between two parallel rigid walls. (a) Evolution snapshot and related isosurface plot of BCP melt system with the ratio of 1:3 between A and B beads, at the time step $t = 5.4 \times 10^3$ for zero shear rate. (b) Snapshot at the same time and zero shear for the BCP melt system with a 1:7 ratio of A and B beads.

Now, we focus on the off-critical BCP melt system with two different ratios of A and B type beads. To compare the results with the previously discussed critical mixture, we have considered two solid walls, one at the top and another at the bottom of the system. We will allow the walls to move in various scenarios, as before. Let's first understand the evolution of these systems without applying shear. We have taken two ratios: 1:3 and 1:7 between A and B type beads in each BCP chain, and the evolution is depicted in Figs. 4.21(a) and 4.21(b), respectively, at $t = 5.4 \times 10^3$.

In an asymmetric BCP melt system, the early evolution resembles the nucleation of A-type beads within the bulk of B-beads. In Fig. 4.21(a), the BCP melt tends to form cylindrical structures; however, we notice an interconnected morphology at the given time interval. In contrast, in Fig. 4.21(b), we observe the peanut-like structure at the specified time interval. If we wait longer, it may develop into complete spherical domains.

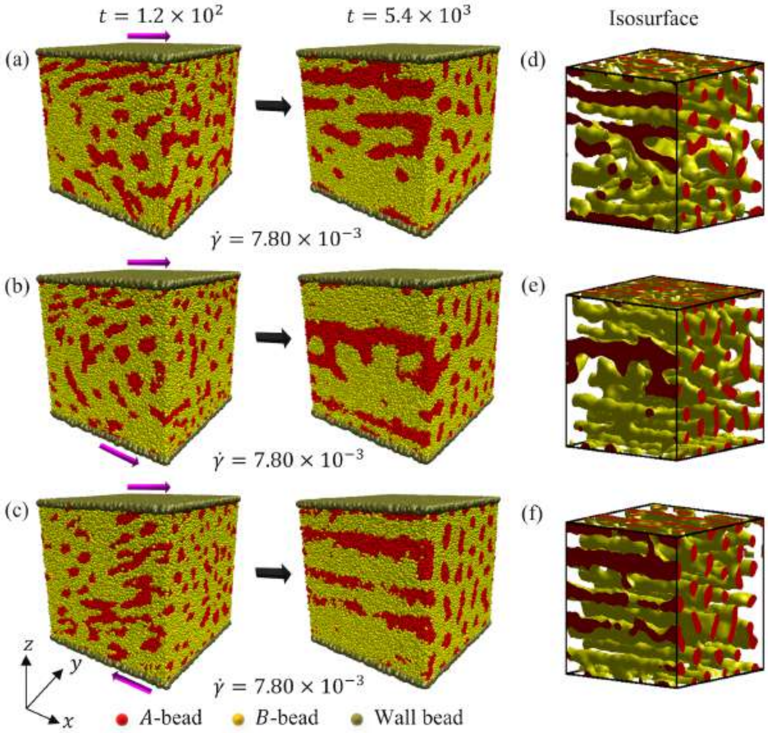

Fig. 4.22: Comparison of the effect of shear in different cases 2-4 in BCP melt system with 1:3 ratio of A and B beads. The evolution snapshots are taken at two different time intervals plotted in the first two columns at $t = 1.2 \times 10^2$ and $t = 5.4 \times 10^3$, respectively. The third column plots the isosurface related to the snapshots at the late time.

In Fig. 4.21(a), we observed the interconnected morphology for the asymmetric BCP melt with a 1:3 ratio. Subsequently, we applied shear to the system at a moderate shear rate of $\dot{\gamma} = 7.80 \times 10^{-3}$ in scenarios 2-4. The related evolution is shown in Fig. 4.22. Upon applying shear, the domains start flowing along the shear direction and starts forming elongated structure. If we compare the late-time evolution in Figs. 4.22(a), 4.22(b), and 4.22(c), the interconnected morphology starts elongating along the x-direction with the increasing effect of shear from cases 2-4. Finally, in cases 3 and 4, where the shear is more effective, perfect cylindrical morphologies are observed oriented along the x-direction. Thus, under the effect of shear, we can achieve cylindrical structures more quickly with perfect ordering.

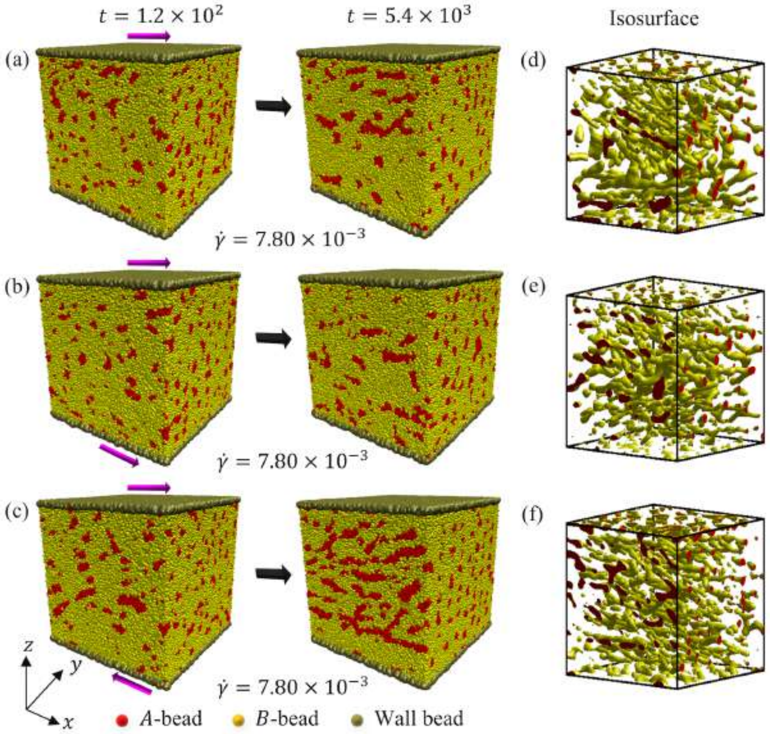

Fig. 4.23: Evolution snapshots of BCP melt system with 1:7 ratio of A and B beads for cases 2-4. The first two columns represent the morphology at $t = 1.2 \times 10^2$ and $t = 5.4 \times 10^3$, respectively. The third column depicts the isosurface corresponding to the evolution shown in column two.

In Fig. 4.23, we illustrate domain evolution for a highly asymmetric mixture of BCP melt with a 1:7 ratio of A and B type beads. We applied a moderate shear rate of $\dot{\gamma} = 7.80 \times 10^{-3}$ and compared the evolution for cases 2-4 at two-time intervals mentioned at the top. Upon applying shear, the A and B domains begin to flow and reorient to minimize its effect. As discussed in the case of the critical BCP melt system, the impact of shear increases from case 2 to case 4. In case 2, where only the top wall is moving, the slabs near the top wall are primarily affected, and elongated domains are observed in this region. As we move to cases 3 and 4, shear is applied from both directions, resulting in more ordered structures formed under the same shear and time intervals. In case 4, the effect of shear is maximum, and we observe the formation of short, distorted cylinders aligned along the x-direction (direction of applied shear). Overall, we observe that with the application of shear, we can tune the morphology of a highly asymmetric BCP melt system from peanut-type structures to short, distorted cylindrical domains.

4.13 Summary and discussion

We have studied the phase separation kinetics of a block copolymer (BCP) melt system using the Dissipative Particle Dynamics (DPD) simulation technique. External shear is applied to the system under three distinct unidirectional shear conditions. The BCP melt is confined between two solid walls, one at the top and the other at the bottom. Shear is introduced by moving these walls at a constant velocity in specific directions. The three shear conditions are as follows: (i) only the top wall moves (case 2), (ii) both walls move in the same direction (case 3), and (iii) both walls move in opposite directions (case 4). We analyze the effect of shear on the evolution of morphology, characterization functions, growth laws, anisotropy development, and other relevant parameters such as velocity profile and viscosity. Additionally, we compare the unidirectional structure factor along different directions and under various shear conditions to evaluate anisotropy development in the system. All these results are compared with a reference case where the walls are stationary, and no shear is applied (case 1).

Upon applying shear, the A and B type clusters start flowing in the direction of wall motion. BCP chains reorient perpendicular to the shear direction to minimize the shear effect, forming lamellar-type structures. The formation of these lamellar structures begins near the moving walls. Compared to the reference case, fully developed lamellar structures are achieved more quickly at high shear rates, whereas, at lower shear rates, well-developed lamellar structures are not observed within the given time intervals. We characterized the morphology under various shear conditions by comparing the radial distribution function (RDF), density profile, scaling functions, and growth laws. In cases 2 and 3, the late-time correlation and structure factor overlap well, indicating the same universality class. However, significant deviations are noted at all shear rates in case 4, where the shear effect is more prominent. The application of shear leads to a more periodic morphology, evidenced by the oscillatory nature of the correlation function and the emergence of secondary peaks in the structure factor curves. Furthermore, the shear thinning of the domains is demonstrated by the broadening of the primary peaks in the structure factor.

A competition emerges between domain coarsening and shear effects upon applying shear, reflected in the length scale curves, leading to intriguing behaviors. Early-time diffusive growth is observed at low shear rates, with phase segregation being dominant in all cases. From the plots of average shear viscosity against shear rates, lower shear thinning is noted at low shear rates, with higher values of shear viscosity. When the length scale in case 1 reaches saturation, the length scale for cases 2 and 3 at lower shear rates also significantly slows within a specific time interval. Conversely, in case 4, negative growth is observed for a prolonged period as shear dominates over diffusive growth. This causes the BCP chains to readjust to minimize the shear effect. Following this, the length scale grows again following diffusive growth and eventually saturates at a value nearly equal to or lower than in case 1 at late times. Furthermore, at moderate and high shear rates, domain coarsening is dominated by shear from the beginning in almost all cases. Consequently, the growth of the length scale slows down from early times and later saturates at lower $R(t)$ values, indicating shear thinning of the domains. The variation of average viscosity over the shear rate further supports this observation.

We have also studied the impact of shear on the asymmetric BCP melt system with two different ratios, 1:3 and 1:7, between A and B particles. As we increase the asymmetry, the formation of cylindrical, spherical, and peanut-type structures are noted. In the reference case of zero shear rate, we observed interconnected and peanut-shaped morphologies for the asymmetric mixtures of 1:3 and 1:7 ratios, respectively. When shear is applied to the system, the microdomains start flowing along the shear directions and readjust themselves to minimize the shear effect. In the first system, with a ratio of 1:3, elongated structure form along the shear direction. Under moderate shear rates in cases 3 and 4, perfect cylindrical structures oriented along the x-direction are formed. In the second mixture with an asymmetric ratio of 1:7, the formation of elongated microdomains is noted, which eventually form short distorted cylinders in case 4, where shear is more effective.

Overall, this study elucidates the impact of shear on the phase separation kinetics of BCP melt systems. The findings can guide the rapid formation of composite materials with diverse and intriguing physical properties. Considering the scientific and technological significance of BCP melt morphologies, these results will spur further experimental and theoretical exploration of this topic. Additionally, this work provides a comprehensive framework for simulating morphology development in BCP melts and polymer blends under external influences.